Title

General model for calcite growth kinetics in the presence of impurity ions

Authors

Nielsen, Laura C

De Yoreo, James J

DePaolo, Donald J

Publication Date

2013-08-01

DOI

10.1016/j.gca.2013.04.001

Co-dependent calcite growth kinetics, inhibition and impurity uptake

Laura C. Nielsen[1*], James J. De Yoreo[2] & Donald J. DePaolo[1,2]

[1]Center for Isotope Geochemistry, University of California-Berkeley, Berkeley, CA, 94720

[2]Lawrence Berkeley National Laboratory, Berkeley, CA, 94720

[*]corresponding author: lnielsen@berkeley.edu

ABSTRACT

The concentrations of Sr, Mg and other elements in calcite are widely used to infer the conditions of mineral growth. However, such inferences are dependent on the mechanisms that govern the incorporation of minor constituents into the calcite lattice during mineral growth. A particularly confusing observation is that both Sr and Mg are readily incorporated into growing calcite crystals at low concentration but inhibit calcite growth at higher concentrations. Here we show that the growth rate dependence of Sr and Mg incorporation into calcite, as well the inhibitory effects on calcite growth, can be predicted with an ion-by-ion crystal growth model where ion attachment is confined to kink sites on the crystal surface.

The exchange of ions between active growth (kink) sites on the mineral surface and aqueous solution governs both the efficiency of incorporation of minor constituents and the kinetics of mineral precipitation. Ions such as Sr and Mg in calcite, that are not stoichiometric constituents, may attach to kink sites and impede crystal growth by either blocking propagation of the kink (kink blocking), or if incorporated into the growing mineral, straining the local crystal lattice, and hence increasing the mineral solubility (incorporation inhibition). Here we investigate the effects of including these growth inhibition mechanisms into a microscopic model for crystal growth based on kink creation, propagation and collision (CPC) theory. This model, while also accounting for the efficiency of impurity ion incorporation, predicts that kink blocking causes an exponential decrease in mineral growth rate with increasing impurity concentration, while incorporation inhibition results in more complicated functional forms of the growth rate effect depending on the thermodynamics of the solid solution. Applying this model to existing data on the partitioning of strontium and magnesium into calcite and the simultaneous effects on growth kinetics and mineral composition, we find that strontium uptake inhibits growth by enhancing mineral solubility while magnesium inhibits growth primarily by kink blocking. Our model should be widely applicable to understanding the impurity content of a large range of sparingly soluble minerals that form by precipitation from aqueous solutions.

1. INTRODUCTION

Impurity ions and ionic molecules are widely known to inhibit the growth and alter the composition of carbonate minerals precipitating from aqueous solution (Meyer, 1984; Burton and Walter, 1990; Cabrera and Vermilyea, 1958; Davis et al., 2000b; Reddy and Hoch, 2000; Wasylenki et al., 2005b,a; Lin and Singer, 2006). Use of trace element signatures for paleoclimate reconstruction, retardation of contaminant transport (Lukashev, 1993), and preventing pipe scaling requires an understanding of controls on impurity incorporation during carbonate mineral growth. Despite the widespread application of trace element signatures, the nonlinear effects of certain trace elements, such as strontium, on calcite precipitation rate have largely eluded explanation (Wasylenki et al., 2005b). No single theory has described growth inhibition by both the kink pinning and incorporation inhibition mechanisms simultaneously. Although significant advances have been made in atomic-scale understanding of growth (Zhang and Nancollas, 1990; Teng et al., 1998; Zhang and Nancollas, 1998; Teng et al., 1999, 2000), rate equation and trace element partitioning models are still empirically-based and relatively crude. While most rate equations ignore the feedbacks between ion incorporation and mineral growth kinetics, impurity uptake affects subsequent growth kinetics and should therefore be treated explicitly.

Precipitation of calcite from natural aqueous fluids leads to the incorporation of numerous trace, non-constituent ions, which affect mineral growth kinetics and composition. Divalent ions of metals including iron (Katz et al., 1993), copper (Parsiegla and Katz, 1999), cadmium, manganese (Lorens, 1981), barium (Tesoriero and Pankow, 1996), magnesium (Plummer and Busenberg, 1987; Davis et al., 2000a,b) and strontium (Tesoriero and Pankow, 1996; Gabitov and Watson, 2006) have been shown to co-precipitate with calcite and to subsequently affect growth rate. Anions including sulphate (Flaathen et al., 2011), phosphate (House and Donaldson, 1986), and uranyl (Reeder et al., 2001) may also be sparingly incorporated into the calcite lattice. In general, increased impurity loading and uptake leads to decreased growth rate (e.g. Meyer, 1984), but in some cases, small amounts of impurity may speed crystallization kinetics (Wasylenki et al., 2005b).

Several models have been proposed to describe the relationship between growth rate and impurity uptake in calcite. Decreased precipitation rate with increasing tracer concentration is generally attributed to a kink blocking mechanism (Wasylenki et al., 2005b) or to increased mineral solubility (Davis et al., 2000) or a combination of both. In the latter case, the overall solubility of the impurity-$CaCO_3$ solid solution is invoked to explain the decrease in growth rate. No model has successfully captured the effect of strontium incorporation on calcite precipitation rate (Wasylenki et al., 2005b), and most models describe qualitative behavior without allowing direct calculation of predicted growth rates and partition coefficients as a function of solution composition.

By accounting for the molecular mechanisms of growth inhibition at the mineral aqueous interface, we derive widely-applicable expressions relating solution composition to precipitation rate and crystal composition. In the case of non-incorporating impurities, these may be solved analytically, while in the nonlinear case of trace element incorporation, numerical solution is required. The expressions predict that kink blocking by strong-adsorbing aqueous species will cause an exponential decrease in mineral precipitation rate with increasing impurity concentration, consistent with classical growth inhibition theory (Cabrera and Vermilyea, 1958) and with Langmuir-type inhibitor adsorption (Weaver et al., 2010). Growth inhibition by the incorporation of trace species into the bulk lattice will be shown to depend on the thermodynamics of solid solution and the rates of trace ion incorporation relative to the constituent ions. We demonstrate the wide applicability of these expressions by modeling calcite growth in the presence of a variety of impurities that have been explored experimentally.

2. UNDERLYING MECHANISMS AND GOVERNING EQUATIONS

The net flux of ions to the mineral surface governs the composition and growth kinetics of precipitating minerals. At ambient temperature and supersaturations not exceeding the solubility of amorphous calcium carbonate (ACC), ion incorporation into calcite occurs primarily at kink sites along step edges at the mineral aqueous interface (DeYoreo et al.,

2009; Larsen et al., 2010; Nielsen et al., 2012). Overall growth occurs when the net rate of ion attachment at kink sites exceeds the net rate of ion detachment. Calcite precipitation from aqueous solution may be described by the creation-propagation-collision (CPC) model, where kink sites are created by the formation of stable 1D nuclei along the step, and propagate (i.e. grow by ion addition from solution) parallel to the step until they disappear by collision with a kink moving in the opposite direction (Zhang and Nancollas, 1990, 1998; Larsen et al., 2010).

Recent studies of calcite growth in the presence of impurities concluded that, for the cases of polyaspartate (Elhadj et al., 2006) and Mg^{2+} (Davis et al., 2000a,b), the observed inhibition is caused by 1) blocking of kink sites by non-incorporated ions or molecules, and 2) incorporation of trace ions or molecules that alter the mineral solubility, respectively. Regardless of the mechanism of inhibition, the relative rates of constituent ion and trace element incorporation control the final bulk calcite composition (DePaolo, 2011; Nielsen et al., 2012) and can thus be related to the relative rates of attachment and detachment by constituent ions and impurities.

2.1. Governing equations

The net rate of ion attachment to kink sites (s^{-1}) is defined by

$$u_i = k_i[i]P_j - \nu_i P_i \tag{2.1}$$

for ion i attaching to a j-type kink site, where $[i]$ is the ion activity in solution, k and ν are the ion attachment ($s^{-1}M^{-1}$) and detachment (s^{-1}) rate coefficients respectively, and P_i is the probability of a given kink site being an i site (Zhang and Nancollas, 1990). We note that rate coefficients of attachment and detachment can be cast in terms of fluxes following,

$$k_i = \phi e^{-E_A/k_b T}, \tag{2.2}$$

where ϕ represents a flux due to Brownian collisions, E_A is the activation energy barrier for reaction (J/mol), k_b is the Boltzmann constant (J mol^{-1} K^{-1}), and T is temperature (K). However, this level of detail is not currently useful given our limited understanding of the energy landscape of relevant reactions. It is thought that kinetics of attachment are dominantly dissociative, controlled by the kinetics of ion or kink site desolvation. Attachment of calcium ions to carbonate kink sites is likely limited by the rate of calcium desolvation, while the rate of carbonate ion attachment may be limited by the rate of calcium kink dehydration (e.g. Larsen et al., 2010). Here we assume that detachment rate coefficients are controlled by the affinity of ions for kinks and are independent of site-type along the step, as was also assumed in other studies (Zhang and Nancollas, 1990, 1998; Elhadj et al., 2006).

In the case of a trace impurity interacting with the growing calcite surface, the attachment kinetics of calcium ion (denoted by A), carbonate ion (denoted by B), and impurity ions (denoted by M) control growth rate. To determine net ion attachment fluxes and therefore growth rate and overgrowth composition, the kink site probabilities (P_A, P_B, and P_M) must be known. Three constraint equations are required to solve for the probabilities of A, B and M kink sites, where M is assumed to attach to carbonate ions and substitute for calcium (A) ions. To preserve crystal stoichiometry, one B ion must attach for each A and M ion. It follows that:

$$u_A = u_{B-A}, \tag{2.3}$$

and

$$u_M = u_{B-M}, \tag{2.4}$$

where u_{B-i} is the net frequency of B attachment to i. Three types of kink sites are defined, so,

$$P_A + P_B + P_M = 1. \tag{2.5}$$

Once kink probabilities and ion attachment frequencies have been determined, the overall growth rate may be calculated from the net ion attachment frequency ($u_{net} = u_A + u_B +$

u_M) following

$$R = \frac{\rho u_{net} hbd}{2y_0} = \frac{v_{st} bd}{y_0} \tag{2.6}$$

where ρ is the kink density, h is the step height (m), b is kink depth (m), d is mineral density (mol/m^3), y_0 is terrace width, and v_{st} (m/s) is the step velocity (Teng et al., 1998; Zhang and Nancollas, 1998; Nielsen et al., 2012). Terrace width may be written,

$$y_0 = \frac{8\Gamma hab\alpha}{k_b T \sigma}, \tag{2.7}$$

where a (m) is molecular unit width along the step, Γ is approximately 1 for calcite, σ is supersaturation (= ln[IAP/K$_{sp}$]) and α (J/m^2) is step edge free energy per unit step height (Teng et al., 1998).

Kink density, ρ, is given by the expression,

$$\rho = \sqrt{\frac{2I}{u_{net}}}, \tag{2.8}$$

where I is the stable 1D nucleation rate (Nielsen et al., 2012). Following Zhang and Nancollas (1990), I may be approximated by,

$$I = P_0 \left(\frac{k_A[A]}{\Omega_A} + \frac{k_B[B]}{\Omega_B} \right), \tag{2.9}$$

where Ω_A^{-1} and Ω_B^{-1} effectively represent acceptance probabilities for A and B kink nucleation, and P_0 is the probability that a given site along the step is a non-kink site ($P_0 = 1 - \rho$; Zhang and Nancollas, 1998). Assuming stable 1D nuclei ultimately grow to infinite length,

$$\Omega_A = 2 + \left(\frac{\nu''_A}{k_B[B]} + \frac{\nu''_A}{k_A[A]} \frac{\nu_B}{k_B[B]} \right) \times \left(1 - \frac{\nu_A \nu_B}{k_A[A] k_B[B]} \right)^{-1}, \tag{2.10}$$

where the detachment frequencies of single ions adsorbed to the step with kink formation energy ϵ (J mol^{-1} K^{-1}) may be expressed $\nu''_A = \nu_A e^{2\epsilon/k_b T}$ and $\nu''_B = \nu_B^{2\epsilon/k_b T}$ (Zhang and

Nancollas, 1998). Upon substitution of Eq. 2.9, Eq. 2.8 simplifies to

$$\rho = \sqrt{(1-\rho) \times C}, \tag{2.11}$$

where

$$C = \frac{2}{u_{net}} \left(\frac{k_A[A]}{\Omega_A} + \frac{k_B[B]}{\Omega_B} \right). \tag{2.12}$$

Kink probability ρ may be determined by solving Eq. 2.11.

The kink formation energy can be obtained from measurements of equilibrium kink spacing. Equilibrium kink spacing (L_{eq}= 1/ρ_{eq}) for a given value of kink formation energy may be calculated by substituting the 1D nucleation rate (Eq. 2.9) and net kink propagation rate into Eq. 2.8, setting [A] and [B] equal to the equilibrium activities of calcium and carbonate ions in solution ($\sqrt{K_{sp}}$). In this calculation, we use the attachment and detachment rate coefficients fitted to Larsen et al. (2010) obtuse step velocities , which may be found in Nielsen et al. (2012). DeYoreo et al. (2009) determined a near-equilibrium kink spacing for calcite of ∼5-7 molecular unit widths at 298 K. An ϵ/k_bT corresponding to the observed spacing is approximately equal to 2.8.

The calcite kink formation energy may also be estimated using the BCF expression for equilibrium kink spacing:

$$L_{eq} = 1 + (1/2)e^{\epsilon/k_bT} \tag{2.13}$$

(Burton et al., 1951; Chernov et al., 2004). If we assume that L_{eq} = 7, we find that ϵ/k_bT estimated in this way is equal to 2.5, which is similar to our calculated value. These estimates of kink formation energy factor are significantly smaller than a prior estimate of ϵ/k_bT = 7.775 (Larsen et al., 2010) based on molecular simulation (Kristensen et al., 2004), which corresponds to an equilibrium kink spacing of 842 molecular unit widths.

2.2. Non-incorporating impurities (kink blocking)

The strong specific adsorption of ions to kink sites on the calcite surface may inhibit growth by preventing the subsequent attachment of calcium or carbonate ions. This class of

calcite growth inhibitors presumably includes large molecules such as polyaspartate (Elhadj et al., 2006) and citrate (DeYoreo et al., 2009) that bind strongly to kink sites but do not fit into the calcite lattice in appreciable amounts. In this case, the concentration of kink-blocking large molecules will reach a steady state or constant value. The net impurity attachment rate will be negligible ($u_M = u_{B-M} = 0$), so kink probabilities can be determined analytically by solving Eqs. 2.3-2.5 using Eq. 2.1. The kink site probabilities are given by

$$P_A = \frac{\nu_M(k_A[A] + \nu_B)}{\nu_M(k_A[A] + k_B[B] + \nu_A + \nu_B) + k_M[M](k_B[B] + \nu_A)}, \tag{2.14}$$

$$P_B = \frac{\nu_M(k_B[B] + \nu_A)}{\nu_M(k_A[A] + k_B[B] + \nu_A + \nu_B) + k_M[M](k_B[B] + \nu_A)}, \tag{2.15}$$

and

$$P_M = \frac{k_M[M](k_B[B] + \nu_A)}{\nu_M(k_A[A] + k_B[B] + \nu_A + \nu_B) + k_M[M](k_B[B] + \nu_A)}, \tag{2.16}$$

which depend solely on the rate coefficients for ion attachment and detachment frequencies (k and ν) and ion activities in solution. The affinity of impurity ions for kink sites will control the kinetics of impurity ion detachment (Elhadj et al., 2006) and thus the efficiency of kink blocking.

Rate coefficients of ion exchange at kink sites k and ν control net ion attachment fluxes and thus the overall precipitation rate. For pure calcite growing in the presence of a kink-blocking impurity, the values for k_A, k_B, ν_A and ν_B may be constrained by the solubility of calcite. At equilibrium, the net attachment fluxes of A and B must be zero. Setting u_A and $u_B = 0$, from 2.1 we find,

$$[A]_{eq} = \frac{\nu_A P_A}{k_A P_B}, \tag{2.17}$$

and

$$[B]_{eq} = \frac{\nu_B P_B}{k_B P_A}. \tag{2.18}$$

The solubility of an AB mineral is equal to the product of equilibrium ion activities, $K_{AB} =$

$[A]_{eq}[B]_{eq}$, so

$$K_{AB} = \frac{\nu_A \nu_B}{k_A k_B}. \tag{2.19}$$

If the rate coefficients of attachment and detachment are equal for ions A and B ($k_A = k_B = k$ and $\nu_A = \nu_B = \nu$), only one fitted parameter is sufficient to determine both k and ν:

$$\nu = \sqrt{K_{AB} k^2}. \tag{2.20}$$

The dependence of calcite growth rate on non-incorporating impurity concentration may be solved following the procedure detailed in Appendix B.

2.3. Incorporation inhibition

We model calcite growth kinetics and composition during precipitation in the presence of impurities using a CPC approach. Net ion attachment rates are determined numerically based on the constraint equations 2.3-2.5. Following Eq. 2.1, the net rate of B ion attachment to A kink sites is expressed,

$$u_{B-A} = k_B[B]P_A - \nu_B P_{B-A}, \tag{2.21}$$

where $P_{B-A} = P_B(1-x)$ is the probability that a carbonate kink site sits adjacent to a calcium along the step, with mole fraction $CaCO_3$ in the solid solution of $(1-x)$. An analogous expression may be written for the net rate of B ion attachment to kink sites occupied by impurities,

$$u_{B-M} = k_{B-M}[B]P_M - \nu_{B-M} P_{B-M}, \tag{2.22}$$

where $P_{B-M} = P_B x$. Carbonate ions may attach to and detach from calcium and impurity kink sites with different frequencies, so the rate coefficients of B ion reaction with A sites may not equal those of B ion reaction with M sites ($k_{B-M} \neq k_B$ & $\nu_{B-M} \neq \nu_B$). The ratio of impurity to calcium in the crystal (r_x) during steady state crystal growth is equal to the

ratio of net impurity and calcium ion attachment rates,

$$r_x = u_M / u_A, \tag{2.23}$$

which is related to the mole fraction of the impurity carbonate by the following relation,

$$x = \frac{r_x}{1 + r_x}. \tag{2.24}$$

2.3.1. Thermodynamics of metal carbonate solid solutions

During the formation of a solid solution between impurity carbonate and calcite, the affinity of ions for kink sites imposes a control on the rate of ion detachment from those sites. We propose that the solubility of each solid solution end-member constitutes a measure of this affinity and may therefore be used to calculate ion detachment frequency ν. Specifically, the detachment frequency of a given ion will depend upon the equilibrium aqueous ion activity corresponding to the endmember component of $M_xA_{1-x}B$, where x is the impurity carbonate mole fraction in the solid solution.

The thermodynamics of metal carbonate solid solutions can be represented with Lippmann diagrams, which portray the thermodynamic relationship between the solid solution and aqueous solution. We refer the reader to Glynn and Reardon (1990) and Gamsjäger et al. (2000) for a comprehensive discussion of Lippmann diagrams.

In the Lippmann construct, the total solubility of a solid solution with mole fraction of impurity carbonate equal to x is defined by a "solidus" equation, which for a metal impurity (M) calcium carbonate, $M_xA_{1-x}B$, may be expressed:

$$\Sigma\Pi = K_{AB} a_{AB} + K_{MB} a_{MB}, \tag{2.25}$$

where $a_{AB} = \gamma_{AB}(1-x)$ and $a_{MB} = \gamma_{MB} x$ are the solid end-member activities with activity coefficients γ, and K_{AB} and K_{MB} are the AB and MB solubilities (Glynn and Reardon, 1990). Total solubility is equivalent to the sum of end-member component equilibrium ion

activity products,

$$\Sigma\Pi = [A]_{eq}[B]_{eq} + [M]_{eq}[B]_{eq}. \tag{2.26}$$

The composition of the aqueous solution at equilibrium with this solid solution phase can be characterized with a corresponding aqueous phase mole fraction (y):

$$y = \frac{[M]_{eq}[B]_{eq}}{[M]_{eq}[B]_{eq} + [A]_{eq}[B]_{eq}}. \tag{2.27}$$

The value of y can be determined from the solutus equation for non-ideal solid solutions (Glynn and Reardon, 1990):

$$\Sigma\Pi = \left(\frac{y}{K_{MB}\gamma_{MB}} + \frac{1-y}{K_{AB}\gamma_{AB}}\right)^{-1}. \tag{2.28}$$

At equilibrium, the ion activity products of AB and MB may be expressed in terms of solid activities or in terms of total solubility ($\Sigma\Pi$) and y,

$$[A]_{eq}[B]_{eq} = (1-x)K_{AB}\gamma_{AB} = \Sigma\Pi \times (1-y), \tag{2.29}$$

and

$$[M]_{eq}[B]_{eq} = xK_{MB}\gamma_{MB} = \Sigma\Pi \times y. \tag{2.30}$$

If the relationship between γ_{AB}, γ_{MB} and the mole fraction of MB in the solid solution (x) is known (in others word, if the thermodynamics of the solid solution are known), the equilibrium activities of A, B and M (calcium, carbonate, and trace metal) ions may be calculated.

2.3.2. Solubility controls on detachment kinetics

The net attachment fluxes of A, B and M must equal zero at equilibrium, so equations for u_A, u_B, u_{B-A} and u_{B-M} (Eqs. 2.1, 2.21, and 2.22) can be reorganized to solve for $[A]_{eq}$, $[B]_{eq}$ and $[M]_{eq}$. Combining these expressions with Eqs. 2.29 and 2.30, the product of ion detachment frequencies for solubilities as a function of the equilibrium ion activity

becomes,

$$\nu_A \nu_B = \frac{[A]_{eq}[B]_{eq} k_A k_B}{1 - x}, \tag{2.31}$$

and

$$\nu_M \nu_{B-M} = \frac{[M]_{eq}[B]_{eq} k_M k_{B-M}}{x}. \tag{2.32}$$

The exact form of solid activity coefficients varies among impurity elements, so the effect of impurity incorporation on detachment frequencies and overall growth kinetics is impurity element-dependent. Increasing the activity coefficient of either solid solution end-member will result in an increased frequency of detachment for its ionic constituents. Variation in ion detachment frequencies is mechanistically related to the effects of lattice strain on bond strength during the incorporation of ions of different sizes. Increasing detachment frequency reflects decreasing affinity of an ion for its kink site.

To minimize the number of parameters, we have assumed that impurity ions in positions other than the currently propagating step do not affect attachment frequencies. Astilleros et al. (2010) observed that the steps propagating across the original, pure calcite substrate maintained higher step velocities than those propagating across the magnesian calcite overgrowth, so this assumption is not strictly valid. However, this effect is transient, and the step velocities reach steady state within a few minutes. The model in its current form captures the primary co-dependencies of growth rate and trace element incorporation; it would be straightforward to add additional complexity once the rate coefficients of ion attachment to and detachment from different types of kink sites are experimentally or computationally accessible.

2.3.3. Partition coefficients

The steady state growth rate and solid solution composition corresponding to a given [A], [B] and [M] can be determined by numerically solving the nonlinear system of equations 2.3-2.5 and 2.21-2.24 (see Appendix C for further detail). With r_x it is trivial to

calculate the observed partition coefficient,

$$K_p = \frac{r_x}{r_s}, \tag{2.33}$$

where $r_s = [M]/[A]$, the concentration ratio of impurity to calcium in solution. If growth occurs at near equilibrium supersaturation, the measured partition coefficient can be related to a thermodynamic equilibrium constant for the ion exchange reaction:

$$M + AB \rightarrow A + MB. \tag{2.34}$$

The equilibrium constant for this reaction is the ratio of impurity to calcium carbonate activities divided by the ratio of impurity to calcium activities in solution,

$$K_{p,eq} = \frac{a_{MB}/a_{AB}}{[M]/[A]} = \frac{K_{AB}}{K_{MB}}, \tag{2.35}$$

which follows from $[A]_{eq}[B]_{eq} = K_{AB}a_{AB}$ and $[M]_{eq}[B]_{eq} = K_{MB}a_{MB}$. This expression can be related to the measured partition coefficient by solid and aqueous activity coefficients, such that

$$K_{p,eq} = K_p \frac{\gamma_{MB}/\gamma_{AB}}{\gamma_P/\gamma_A}, \tag{2.36}$$

where γ_i is the activity coefficient for solid or aqueous species i (Morse and Bender, 1990; Rimstidt et al., 1998).

3. EXAMPLES OF MODEL APPLICATION

In the following section, the equations presented above are used to model calcite growth from aqueous solutions containing three types of impurities: the non-incorporating impurity, polyaspartate, and two key trace constituents of calcite, strontium and magnesium. These impurities were selected because of the availability of high quality atomic force microscope (AFM) step velocity data. Divalent cations of strontium and magnesium also

bracket Ca^{2+} in size, illustrating the effects of large and small cation substitution on calcite growth kinetics.

3.1. Kink inhibition by polyaspartate

Elhadj et al. (2006) performed a series of calcite precipitation experiments varying the concentrations of several polyaspartates with varying affinity to kink sites on the calcite surface. Polyaspartates are protein components found in biomineralizing organisms, which are thought to control crystal morphology through specific interactions with the calcite surface (Elhadj et al., 2006). With an exponential increase in polyaspartate concentration, the rate of calcite precipitation remains relatively constant (polyaspartate-1 and -2) or increases slightly (polyaspartate-4, -5 and -6) until a certain threshold concentration is reached. Above this threshold, step velocity plummets to zero. Figure 1 illustrates the observed dependence of obtuse step velocity on polyaspartate-1 and -2 concentrations with the corresponding model curve using parameters listed in Table 1.

[Figure 1 about here.]

[Table 1 about here.]

Two significant effects of polyaspartate on calcite obtuse step velocity are not captured by the model in its most basic form: 1) increasing step velocity with increasing polyaspartate concentration and 2) complete step stoppage at sufficiently high [Asp]. The increased step velocity with increasing [Asp] is observed for longer-chain polyaspartates and cannot be modeled when the rate coefficients for calcium and carbonate attachment are assumed to be constant. However, disruption of the mineral surface solvation structure by adsorbed polyaspartate molecules could labilize sorbed water at the surface, thereby accelerating ion attachment and growth (Elhadj et al., 2006; Piana et al., 2007; Chen et al., 2011). It is possible to model the complete stoppage of step growth by assuming that the rate of 1D nucleation (I) goes to zero when the average distance between kinks is less than the width of the footprint of a given polyaspartate molecule along the step (Fig. 1, dotted line), at

which point the entire step is effectively coated with the impurity and there are no exposed active kink sites where crystal growth can continue.

For slowly adsorbing impurities including certain peptides (Friddle et al., 2010; Weaver et al., 2010), terrace lifetime may not exceed the time to equilibrate the adsorbed impurity concentration. These effects may lead to unexpected non-linear step kinetics that, in turn, should impact impurity incorporation (Friddle et al., 2010; Weaver et al., 2010). Such disequilibrium adsorption adsorption does not appear to affect polyaspartate adsorption to calcite but may affect the kinetics of calcite growth inhibition by other common organic molecules.

3.2. Strontium in calcite

Strontium occurs as a trace element in near-surface terrestrial fluids. Its uptake in calcite is of interest to the scientific community as a potential reservoir for the radioactive contaminant ^{90}Sr (Lukashev, 1993), and the thermodynamics of the calcite-$SrCO_3$ solid solution is well-studied (e.g. Kulik et al., 2010, and references therein). The partitioning of strontium into calcite is rate dependent (Lorens, 1981; Tesoriero and Pankow, 1996; Gabitov and Watson, 2006), and the rate dependence has been attributed to aqueous (Rimstidt et al., 1998) and solid state diffusion (Gabitov and Watson, 2006) effects. Although strontium carbonate forms an aragonitic-type structure at low temperatures, and rhombohedral $SrCO_3$ does not exist in nature, Sr^{2+} substituted into calcite is 6-fold coordinated with oxygen (Pingitore et al., 1992). Thus, the thermodynamics of $Sr_xCa_{1-x}CO_3$ solid solutions relies upon determinations of the hypothetical rhombohedral $SrCO_3$ solubility (Böttcher, 1997; Kulik et al., 2010). The proposed equilibrium solubility of this phase ranges from $10^{-6.1}$ to $10^{-8.2}$, with most estimates being close to $10^{-7.6}$.

[Figure 2 about here.]

To calculate detachment frequencies of strontium and calcium ions during $Sr_xCa_{1-x}CO_3$ solid solution formation, the equilibrium ion activity products $[Sr^{2+}]_{eq}[CO_3^{2-}]_{eq}$ and $[Ca^{2+}]_{eq}$-$[CO_3^{2-}]_{eq}$ must be determined. For the strontium-calcite rhombohedral solid solution, these

ion activity products can be equated to the product of end-member solubilities and activities following Eqs. 2.29 and 2.30:

$$[Ca^{2+}]_{eq}[CO_3^{2-}]_{eq} = (1-x)\gamma_{CaCO_3}K_{CaCO_3}, \tag{3.1}$$

and

$$[Sr^{2+}]_{eq}[CO_3^{2-}]_{eq} = x\gamma_{SrCO_3}K_{SrCO_3}, \tag{3.2}$$

where γ_{CaCO_3}, γ_{SrCO_3}, K_{CaCO_3} and K_{SrCO_3} are the activity coefficients and solubilities of the calcite and rhombohedral $SrCO_3$ end-members respectively (Plummer and Busenberg, 1987; Astilleros et al., 2003). The rhombohedral $SrCO_3$-calcite solid solution can be modeled as a regular solution, with mixing parameter (a_0) ranging from 1.1 to 3.2 (Kulik et al., 2010). The activity coefficient of each regular solution end-member component i and j can be approximated by the following expressions:

$$\gamma_i = exp(a_0 x_j^2), \tag{3.3}$$

and,

$$\gamma_j = exp(a_0 x_i^2), \tag{3.4}$$

where x_i and x_j are the mole fractions of components i and j in the solid solution.

[Table 2 about here.]

A Lippmann diagram depicting the solidus (Eq. 2.25) and solutus (Eq. 2.28) of rhombohedral strontian calcite is shown in Fig. 2. With small amounts of Sr incorporation, the total solubility of the $Sr_xCa_{1-x}CO_3$ solid solution increases substantially. The steeply rising solutus indicates that the increase in solubility is due in large part to enhanced solubility of the $CaCO_3$ end-member. The detachment frequency of Ca^{2+} ions depends upon the $CaCO_3$ ion activity product and therefore increases with increasing mole fraction $SrCO_3$ (Eq. 2.31). This pattern indicates that Sr uptake weakens Ca bonds within the calcite lattice.

[Figure 3 about here.]

Step velocities (Fig. 3; Wasylenki et al., 2005b) and partition coefficients (Fig. 4; Gabitov and Watson, 2006) were modeled as a function of supersaturation and Sr/Ca ratios in solution. Strontian calcite step velocities were calculated as a function of solution composition from Eq. 2.6 using net kink propagation rates calculated by numerically solving for u_{Sr}, u_{Ca}, and u_{CO_3} (Eqs. 2.3-2.5 and 2.21-2.22). Details of the numerical methods are in Appendix C. Detachment rate coefficients were recalculated based on Eqs. 2.31 and 2.32 for each aqueous solution and the corresponding steady state solid composition. Partition coefficients were then calculated from the steady state solid composition based on Eq. 2.23 and 2.33. The model converges to an equilibrium partition coefficient around $K_p = 0.03$, which is close to the value estimated by Fantle and DePaolo (2006), $K_p \sim 0.02$, for calcite equilibrated with deep sea pore fluid.

Data fitting was optimized using the method of steepest descent. Fitted values for thermodynamic parameters a_0 and K_{SrCO_3} (rhombohedral) were limited to the range of values reported in Kulik et al. (2010). No constraints on kinetic parameters for strontium attachment to kink sites exist in the literature, so we allowed them to vary. The highest observed Sr distribution coefficient at 25 °C is approximately 0.3 (Gabitov and Watson, 2006), so we assigned this value to the kinetic end-member partition coefficient (= $k_{Sr^{2+}}/k_{Ca^{2+}}$) which is the fast growth rate limit of the partition coefficient. It is possible that this threshold value could represent transport limitation, where strontium diffuses more slowly than calcium to the mineral surface, instead of limitation by ion attachment rates to kinks. Because Sr^{2+} is weakly hydrated (relative to Ca^{2+}) in solution, it is expected that $k_{Sr^{2+}}$ might approach or even exceed $k_{Ca^{2+}}$, but this is not supported by observed Sr partitioning into rapidly precipitated calcite (Gabitov and Watson, 2006). Further experiments may be necessary to constrain the absolute kinetic end-member partition coefficient for strontium. Fitted solubility, attachment, and detachment rate coefficient parameters are listed in Table 2. Fits to step velocity data from Wasylenki et al. (2005b) and to strontium partitioning data compiled by Gabitov and Watson (2006) are displayed in Figs. 3 and 4 respectively.

The model presented here is the first to successfully fit the step velocity data of Wasylenki et al. (2005b). The calcite step velocity increases slightly at low Sr concentrations and drops off abruptly once a threshold concentration is reached (Fig. 3). The slight increase in growth rate at low strontium concentration occurs because Sr incorporation contributes to the overall precipitation rate. With sufficiently large amounts of Sr incorporation, the total solubility of the mineral exceeds the concentration of constituent ions in solution. At this point, the net rate of calcium and carbonate ion attachment approaches 0, causing the observed abrupt drop in mineral precipitation rate with increasing aqueous strontium.

[Figure 4 about here.]

By reducing solid solution precipitation to its constituent reactions, we are able to identify the mechanisms controlling the nonlinear relationship between step velocity and aqueous strontium concentration. Carbonate ions attach readily to kink sites occupied by strontium ions, so strontium ions do not inhibit growth via a kink blocking mechanism. Strontium incorporation enhances the detachment kinetics of calcium and carbonate ions – likely by causing strain on the crystal lattice – inhibiting growth at relatively low Sr concentrations. Furthermore, strontium uptake decreases the detachment rate coefficient for Sr ions, suggesting that the lattice strain promotes the stability of the $SrCO_3$ solid solution end-member. These combined effects cause runaway Sr uptake and an abrupt decline in growth rate with increasing strontium activity in solution.

[Figure 5 about here.]

3.3. Magnesium in calcite

Magnesian calcite is ubiquitous in terrestrial settings, and magnesium partitioning into calcite is a key paleotemperature proxy. Numerous experimental studies indicate that there is no growth rate dependence of K_p for magnesian calcite over a wide range of supersaturations (Mucci and Morse, 1984; Mucci et al., 1985; Morse and Bender, 1990; Hartley and Mucci, 1996), from $\sigma = 0.18$ to $\sigma = 2.8$. It has been proposed that this occurs because Mg

reaches exchange equilibrium with calcium at the surface (Mucci et al., 1985). This theory contrasts with the notion that the formation of high-magnesian calcite and dolomite are kinetically inhibited (cf. Morse et al., 2007). Magnesium partitions into bulk calcite from seawater with $K_p \sim 0.016$.

[Table 3 about here.]

[Table 4 about here.]

The thermodynamics of the Mg-calcite solid solution has been widely studied, and Lippmann diagrams effectively capture the relationship between equilibrium solid and aqueous compositions for magnesian calcite (Königsberger and Gamsjäger, 1992). Solid compositions obtained during precipitation experiments correspond exactly to the modeled solidus equation (Eq. 2.25) using the following activity coefficient formulations, which are different from those of the simple regular solution model used above for Sr-Ca solid solutions:

$$\gamma_{CaCO_3} = e^{(-\epsilon'/2)x^2}, \tag{3.5}$$

and

$$\gamma_{MgCO_3} = e^{ln(\gamma_\infty)+\epsilon' x-(\epsilon'/2)x^2}. \tag{3.6}$$

Thermodynamic parameters for the Lippmann diagram of the Mg-calcite system used in Fig. 5 are listed in Table 3. Experimentally determined solution compositions do not correspond to the solutus curve (Fig. 5), indicating that the experimental results do not represent thermodynamic equilibrium. Estimates of true equilibrium magnesium partitioning into calcite based on marine carbonate sediments and their corresponding pore fluids ($\sim$0.001; Fantle and DePaolo, 2006) are significantly less than the equilibrium partition coefficients predicted from laboratory experiments (e.g. Mucci and Morse, 1984; Oomori et al., 1987; Lea et al., 1999).

[Figure 6 about here.]

[Figure 7 about here.]

We have modeled the dependence of magnesian calcite growth rate (Figs. 6 and 7) and magnesium partitioning (Fig. 8) on Mg concentration in solution following the procedure detailed in Appendix C using fitted kinetic parameters listed in Table 4. Ion attachment rate coefficients are controlled primarily by desolvation kinetics, and the Mg^{2+} ion desolvates much more slowly than Ca^{2+} in aqueous solution, thus the fitted $k_{Mg^{2+}}/k_{Ca^{2+}}$ is much less than 1. Detachment rate coefficients were calculated by inserting γ_{CaCO_3} and γ_{MgCO_3} into Eqs. 2.31 and 2.32. Varying γ_∞ affects the calculated Mg partition coefficient at low supersaturations (Fig. 8). Using a value of γ_∞ of 1.2 yields a nearly constant ratio of Mg and Ca detachment rate coefficients and consequently results in partition coefficients with little supersaturation (or growth rate) dependence. In any case, Mg partition coefficients obtained from natural and experimental precipitates likely reflect kinetic end-member partitioning, where magnesium uptake is limited by desolvation kinetics. The observed T dependence of magnesium partitioning (Oomori et al., 1987; Lea et al., 1999), then, may be due to changes in the relative rates of Ca^{2+} and Mg^{2+} ion desolvation. Higher temperature will promote magnesium desolvation and thus Mg uptake at kink sites.

[Figure 8 about here.]

Fitting the step velocity data of Astilleros et al. (2010) requires that the rate coefficient of carbonate ion attachment to Mg be much smaller than the coefficient of Mg attachment (Table 4). The exponential drop in precipitation rate with increasing Mg activity suggests that magnesium inhibits calcite precipitation via a combined kink blocking and solubility mechanism. Magnesium attachment inhibits the subsequent attachment of carbonate, much like the blocking of a kink by a non-incorporating impurity. The total solubility and equilibrium ion activity product of $MgCO_3$ increase significantly with Mg incorporation, but the solubility of the calcite end-member, $[Ca^{2+}]_{eq}[CO_3^{2-}]_{eq}$, does not change significantly with Mg uptake. Instead, the calcite end-member behaves as it would in a non-ideal so-

lution with small positive deviations from ideality, where γ_{CaCO_3} remains close to 1 up to relatively high magnesium contents.

[Figure 9 about here.]

The model we have developed based on the Astilleros experimental data is not consistent with the linear dependence of calcite step velocities on aqueous magnesium activity reported in Davis et al. (2000a,b). Astilleros et al. (2010) point out that steps growing upon the original (Mg-free) substrate propagate much more quickly than those precipitating on overgrowth, which are typically rough. It is possible that the Davis et al. (2000a) step velocities were recorded before a steady state growth rate was reached, where steps propagate over substrate of the same composition. This scenario is unlikely, because step propagation rates were relatively high. Davis et al. (2000a,b) use a 0.1M NaCl electrolyte solution in their experiments, while Astilleros et al. (2010) add no additional salts to their solutions. At low supersaturations, NaCl may inhibit precipitation. The complete stoppage of steps observed by Davis et al. (2000a,b) at low magnesium concentrations could possibly be due to kink pinning by the "background" electrolyte NaCl (Weaver et al., 2007). The calcite precipitated by Astilleros et al. (2010) continued growing even at very high magnesium concentrations.

If the assumption that detachment rate coefficients are controlled by thermodynamic equilibrium ion activity products is relaxed, it is possible to model the dependence of step velocity on Mg activity observed by Davis et al. (2000a,b). In this case, we need to assume that all detachment rate coefficients are equal, and calculate ν from the stoichiometric solubility of magnesian calcite ($K_{ss} = ([Mg^{2+}]_{eq}[CO_3^{2-}]_{eq})^x([Ca^{2+}]_{eq}[CO_3^{2-}]_{eq})^{1-x}$), where $[Mg^{2+}]_{eq}[CO_3^{2-}]_{eq} = \frac{\nu^2 x}{k_{Mg^{2+}} k_{CO_3^{2-}-Mg^{2+}}}$, and $[Ca^{2+}]_{eq}[CO_3^{2-}]_{eq} = \frac{\nu^2(1-x)}{k_{Ca^{2+}} k_{CO_3^{2-}}}$ (from Eqs. 2.31 and 2.32). Alternative model fits to Davis et al. (2000b) data are shown in Fig. 9. If the same procedure is used to model Sr incorporation, however, it becomes impossible to model the observed dependence of strontian carbonate step velocity on Sr in solution. We conclude therefore that it is more appropriate to model solid solution formation assuming kink detachment kinetics are controlled by the activity of each endmember.

3.4. Comparison of Sr and Mg inhibition effects

The inhibitory effects of strontium and magnesium on calcite growth are different. Strontium uptake has little effect on calcite growth kinetics until a threshold strontium concentration is reached. Precipitation then abruptly halts as the solid solution becomes undersaturated. Magnesium adsorption exponentially decreases the rate of calcite precipitation even at very low concentrations. With increasing magnesium concentration in solution, calcite step velocities have been shown to level off (Astilleros et al., 2010). The differences in inhibitory action may be attributed to the varying mechanisms of inhibition.

To compare the effects of Sr and Mg on calcite kink dynamics, we have plotted the Ca^{2+} detachment rate coefficient as a function of impurity mole fraction in the solid solution (Fig. 10; from Eqs. 2.31 and 3.1). Increasing x_{SrCO_3} causes a significant increase in the solubility of the $CaCO_3$ end-member and therefore accelerates the kinetics of calcium detachment. Magnesium uptake, on the other hand, stabilizes Ca^{2+} kinks slightly. The observed exponential decrease in step velocity with increasing Mg, then, must be due to blocking of kinks by Mg ions.

[Figure 10 about here.]

4. CONCLUSIONS

Calcite precipitation from natural aqueous fluids usually results in the formation of solid solutions, where impurities substitute for Ca^{2+} or CO_3^{2-} in the mineral lattice. Even in the absence of impurity uptake, precipitation kinetics are typically slower in natural fluids than in simple growth solutions due to the blocking of active growth sites by adsorbed ions or molecules. Although impurity uptake and its inhibitory effects on mineral growth rate are widely observed, it has been difficult until now to formulate a model that accounts for the processes that retard growth. We demonstrated that the effects of both non-incorporated and incorporated impurities on calcite growth kinetics can be modeled using the same framework, where growth rate and composition are controlled by net ion attachment to kink sites.

Incorporation of trace elements into the calcite lattice affects the mineral solubility and therefore bond energies and ion detachment kinetics. The equilibrium ion activity products of solid solution end-member components are controlled by the net fluxes of ions to and from kink sites. Using a regular solution model for strontian calcite, we are able to model the nonlinear relationship between aqueous strontium and step velocity observed by Wasylenki et al. (2005b). Using the same model, we are able to capture the exponential decrease in step velocity with increasing magnesium concentration observed by Astilleros et al. (2010). In the former case, strontium uptake causes the calcium activity coefficient to increase, which subsequently enhances the detachment rates of calcium ions and ultimately destabilizes calcite relative to the solution and stops its growth. The growth rates of strontian calcite is solubility controlled. Magnesium uptake has little effect on the activity coefficient of calcium, so solubility does not control the effects of Mg on growth inhibition on calcite. Instead, Mg^{2+} ions must effectively act as kink blockers. This interpretation of the mechanism of Mg growth inhibition in calcite is not consistent with the findings of Davis et al. (2000b), who observed a linear decrease in step velocity with increasing aqueous magnesium. It is unclear whether the results of Davis et al. (2000b) or Astilleros et al. (2010) are correct, but only the Astilleros et al. (2010) results are consistent with the model presented here.

The kinetic steady state model describing the effects of impurities on calcite growth kinetics and composition derived here is widely applicable to natural carbonates. The constraint equations (Eqs. 2.3-2.5) can be generalized to three or more component solid solutions if the appropriate thermodynamic relations are known. To ensure the predictive power of this model, independent constraints on attachment and detachment rate coefficients – and the dependence of these parameters on solution compositional variables such as ionic strength – are required. Future *in situ* AFM growth experiments, aqueous cluster experiments, and corresponding molecular simulations may be useful to extend our mechanistic understanding of controls on ion fluxes at kink sites. These experimental and computational efforts will be critical for moving us towards a fully molecular description of the

macroscopic growth rates and mineral compositions sampled in natural systems.

REFERENCES

Astilleros J.M., Pina C.M., Fernández-Díaz L., and Putnis A. (2003) Metastable phenomena on calcite $\{1014\}$ surface growing from Sr^{2+}–Ca^{2+}–CO_3^{2-} aqueous solutions. *Chem. Geol.* **193**, pp. 93–107.

Astilleros J.M., Fernández-Díaz L., and Putnis A. (2010) The role of magnesium in the growth of calcite: An AFM study. *Chem. Geol.* **271**, pp. 52–58.

Berner R.A. (1965) Activity coefficients of bicarbonate, carbonate and calcium ions in sea water. *Geochim. Cosmochim. Acta* **29**, pp. 947–965.

Böttcher M.E. (1997) Comment on "Solid solution partitioning of Sr^{2+}, Ba^{2+}, and Cd^{2+} to calcite" by A. J. Tesoriero and J. F. Pankow. *Geochim. Cosmochim. Acta* **61**(3), pp. 661–662.

Burton E.A. and Walter L.M. (1990) The role of pH in phosphate inhibition of calcite and aragonite precipitation rates in seawater. *Geochim. Cosmochim. Acta* **54**, pp. 797–808.

Burton W.K., Cabrera N., and Frank F.C. (1951) The growth of crystals and the equilibrium structure of their surfaces. *Philos. Tr. R. Soc. A* **243**(866), pp. 299–358.

Cabrera N. and Vermilyea D.A. (1958) Growth of crystals from solution. *Growth and Perfection of Crystals* (ed. R.H. Doremus), Wiley, New York, pp. 393–410.

Chen C.L., Qi J., Zuckermann R.N., and Yoreo J.J.D. (2011) Engineered biomimetic polymers as tunable agents for controlling $CaCO_3$ mineralization. *J. Am. Chem. Soc.* **133**, pp. 5214–5217.

Chernov A.A., Yoreo J.J.D., Rashkovich L.N., and Vekilov P.G. (2004) Step and kink dynamics in inorganic protein crystallization. *MRS Bulletin* , pp. 927–934.

Davis K.J., Dove P.M., and Yoreo J.J.D. (2000a) Resolving the control of magnesium on calcite growth: Thermodynamic and kinetic consequences of impurity incorporation for biomineral formation. *Mat. Res. Soc. Symp.* **620**, pp. M9.5.1–M9.5.7.

Davis K.J., Dove P.M., and Yoreo J.J.D. (2000b) The role of Mg^{2+} as an impurity in calcite growth. *Science* **290**, pp. 1134–1137.

DePaolo D. (2011) Surface kinetic model for isotopic and trace element fractionation during precipitation of calcite from aqueous solutions. *Geochim. Cosmochim. Acta* **75**(4), pp. 1039–1056.

DeYoreo J.J., Zepeda-Ruiz L.A., Friddle R.W., Qiu S.R., Wasylenki L.E., Chernov A.A., Gilmer G.H., and Dove P.M. (2009) Rethinking classical crystal growth models through molecular scale insights: consequences of kink-limited kinetics. *Cryst. Growth Des.* **9**, pp. 5135–5144.

Elhadj S., Salter E.A., Wierzbicki A., DeYoreo J.J., Han N., and Dove P.M. (2006) Peptide controls on calcite mineralization: Polyaspartate chain length affects growth kinetics and acts as a stereochemical switch on morphology. *Cryst. Growth Des.* **6**(1), pp. 197–201.

Fantle M.S. and DePaolo D.J. (2006) Sr isotopes and pore fluid chemistry in carbonate sediment of the Ontong Java Plateau: Calcite recrystallization rates and evidence for a rapid rise in seawater Mg over the last 10 million years. *Geochim. Cosmochim. Acta* **70**, pp. 3883–3904.

Flaathen T.K., Oelkers E.H., Gislason S.R., and Aagaard P. (2011) The effect of dissolved sulphate on calcite precipitation kinetics and consequences for subsurface CO_2 storage. *Energy Procedia* **4**, pp. 5037–5043.

Friddle R.W., Weaver M.L., Qiu S.R., Wierzbicki A., Casey W.H., and Yoreo J.J.D. (2010) Subnanometer atomic force microscopy of peptide-mineral interactions links clustering and competition to acceleration and catastrophe. *Proc. Nat. Acad. Sci.* **107**, pp. 11–15.

Gabitov R.I. and Watson E.B. (2006) Partitioning of strontium between calcite and fluid. *Geochem. Geophys. Geosys.* **7**(11), pp. 1–12.

Gamsjäger H., Königsberger E., and Preis W. (2000) Lippmann diagrams: Theory and application to carbonate systems. *Aquatic Geochem.* **6**, pp. 119–132.

Glynn P.D. and Reardon E.J. (1990) Solid-solution aqueous-solution equilibria: Thermodynamic theory and representation. *Am. J. Sci.* **290**, pp. 164–201.

Harstad A.O. and Stipp S.L.S. (2007) Calcite dissolution: Effects of trace cations naturally present in Iceland spar calcites. *Geochim. Cosmochim. Acta* **71**, pp. 56–70.

Hartley G. and Mucci A. (1996) The influence of P_{CO_2} on the partitioning of magnesium in calcite overgrowths precipitated from artificial seawater at 25° and 1 atm total pressure. *Geochim. Cosmochim. Acta* **60**(2), pp. 315–324.

House W.A. and Donaldson L. (1986) Adsorption and coprecipitation of phosphate on calcite. *J. Colloid Interface Sci.* **112**, pp. 309–324.

Huang Y.M. and Fairchild I.J. (2001) Partitioning of Sr^{2+} and Mg^{2+} into calcite under karst-analogue experimental conditions. *Geochim. Cosmochim. Acta* **65**, pp. 47–62.

Katz J.L., Reick M.R., Herzog R.E., and Parsiegla K.I. (1993) Calcite growth inhibition by iron. *Langmuir* **9**, pp. 1423–1430.

Königsberger E. and Gamsjäger H. (1992) Solid-solute phase equilibria in aqueous solution: VII. A re-interpretation of magnesian calcite stabilities. *Geochim. Cosmochim. Acta* **56**, pp. 4095–4098.

Kulik D.A., Vinograd V.L., Paulsen N., and Winkler B. (2010) (Ca,Sr)CO_3 aqueous-solid solution systems: From atomistic simulations to thermodynamic modeling. *Phys. Chem. Earth* **35**, pp. 217–232.

Larsen K., Bechgaard K., and Stipp S.L.S. (2010) Modelling spiral growth at dislocations and determination of critical step lengths from pyramid geometries on calcite surfaces. *Geochim. Cosmochim. Acta* **74**(2), pp. 558–567.

Lea D.W., Mashiotta T.A., and Spero H.J. (1999) Controls on magnesium and strontium uptake in planktonic foraminifera determined by live culturing. *Geochim. Cosmochim. Acta* **63**, pp. 2369–2380.

Lin Y. and Singer P.C. (2006) Inhibition of calcite precipitation by orthophosphate: Speciation and thermodynamic considerations. *Geochim. Cosmochim. Acta* **70**, pp. 2530–2539.

Lorens R.B. (1981) Sr, Cd, Md and Co distribution coefficients in calcite as a function of calcite precipitation rate. *Geochim. Cosmochim. Acta* **45**, pp. 553–561.

Lukashev V.K. (1993) Some geochemical and environmental aspects of the Chernobyl nuclear accident. *Appl. Geochem.* **8**, pp. 419–436.

Meyer H.J. (1984) The influence of impurities on the growth rate of calcite. *J. Cryst. Growth* **66**, pp. 639–646.

Morse J.W. and Bender M.L. (1990) Partition coefficients in calcite: Examinations of factors influencing the validity of experimental results and their application to natural systems. *Chem. Geol.* **82**, pp. 265–277.

Morse J.W., Arvidson R.S., and Lüttge A. (2007) Calcium carbonate formation and dissolution. *Chem. Rev.* **107**, pp. 342–381.

Mucci A. and Morse J.W. (1984) The solubility of calcite in seawater solutions of various magnesium concentration, I_t = 0.697 m at 25°C and one atmosphere total pressure. *Geochim. Cosmochim. Acta* **48**, pp. 815–822.

Mucci A., Morse J.W., and Kaminsky M.S. (1985) Auger spectroscopy analysis of magnesian calcite overgrowths precipitated from seawater and solutions of similar composition. *Am. J. Sci.* **285**, pp. 289–305.

Nielsen L.C., DePaolo D.J., and Yoreo J.J.D. (2012) Self-consistent ion-by-ion growth model for kinetic isotope fractionation during calcite precipitation. *Geochim. Cosmochim. Acta* **86**, pp. 166–181.

Oomori T., Kaneshima H., and Maezato Y. (1987) Distribution coefficient of Mg^{2+} ions between calcite and solution at 10-50°C. *Mar. Chem.* **20**, pp. 327–336.

Parsiegla K.I. and Katz J.L. (1999) Calcite growth inhibition by copper(II) I. Effect of supersaturation. *J. Cryst. Growth* **200**, pp. 213–226.

Piana S., Jones F., and Gale J.D. (2007) Aspartic acid as a crystal growth catalyst. *Cryst. Eng. Comm.* **9**, pp. 1187–1191.

Pingitore N.E., Lytle F.W., Davies B.M., Eastman M.P., Eller P.G., and Larson E.M. (1992) Mode of incorporation of Sr^{2+} in calcite: Determination by X-ray absorption spectroscopy. *Geochim. Cosmochim. Acta* **56**, pp. 1531–1538.

Plummer L.N. and Busenberg E. (1987) Thermodynamics of aragonite-strontianite solid solutions: Results from stoichiometric solubility. *Geochim. Cosmochim. Acta* **51**, pp. 1393–1411.

Reddy M.M. and Hoch A.R. (2000) Calcite crystal growth rate inhibition by aquatic humic substantces. *Advances in Crystal Growth Inhibition Technologies* (ed. Amjad), Kluwer Academic/Plenum Publishers, New York, pp. 107–121.

Reeder R.J., Nugent M., Tait C.D., Morris D.E., Heald S.M., Beck K.M., Hess W.P., and Lanzirotti A. (2001) Coprecipitation of Uranium (VI) with Calcite: XAFS, micro-XAS, and luminescence characterization. *Geochim. Cosmochim. Acta* **65**(20), pp. 3491–3503.

Rimstidt J.D., Balog A., and Webb J. (1998) Distribution of trace elements between carbonate minerals and aqueous solutions. *Geochim. Cosmochim. Acta* **62**(11), pp. 1851–1863.

Teng H.H., Dove P.M., Orme C.A., and DeYoreo J.J. (1998) Thermodynamics of calcite growth: Baseline for understanding biomineral formation. *Science* **282**(5389), pp. 724–727.

Teng H.H., Dove P.M., and DeYoreo J.J. (1999) Reversed calcite morphologies induced by microscopic growth kinetics: Insight into biomineralization. *Geochim. Cosmochim. Acta* **63**(17), pp. 2507–2512.

Teng H.H., Dove P.M., and DeYoreo J.J. (2000) Kinetics of calcite growth: Surface processes and relationships to macroscopic rate laws. *Geochim. Cosmochim. Acta* **13**, pp. 2255–2266.

Tesoriero A.J. and Pankow J.F. (1996) Solid solution partitioning of Sr^{2+}, Ba^{2+}, and Cd^{2+} to calcite. *Geochim. Cosmochim. Acta* **60**(6), pp. 1053–1063.

Wasylenki L.E., Dove P.M., and DeYoreo J.J. (2005a) Effects of temperature and transport conditions on calcite growth in the presence of Mg^{2+}: Implications for paleothermometry. *Geochim. Cosmochim. Acta* **69**(17), pp. 4227–4236.

Wasylenki L.E., Dove P.M., Wilson D.S., and DeYoreo J.J. (2005b) Nanoscale effects of strontium on calcite growth: An in situ AFM study in the absence of vital effects. *Geochim. Cosmochim. Acta* **69**(12), pp. 3017–3027.

Weaver M.L., Qiu S.R., Hoyer J.R., Casey W.H., Nancollas G.H., and Yoreo J.J.D. (2007) Inhibition of calcium oxalate monohydrate growth by citrate and the effect of the background electrolyte. *J. Cryst. Growth* **306**, pp. 135–145.

Weaver M.L., Qiu S.R., Friddle R.W., Casey W.H., and Yoreo J.J.D. (2010) How the overlapping time scales for peptide binding and terrace exposure lead to nonlinear step dynamics during growth of calcium oxalate monohydrate. *Cryst. Growth Des.* **10**, pp. 2954–2959.

Zhang J. and Nancollas G.H. (1990) Kink densities along a crystal surface step at low temperatures and under nonequilibrium conditions. *J. Crystal Growth* **106**, pp. 181–190.

Zhang J.W. and Nancollas G.H. (1998) Kink density and rate of step movement during growth and dissolution of an AB crystal in a nonstoichiometric solution. *J. Colloid Interface Sci.* **200**(1), pp. 131–145.

APPENDIX A. VARIABLE INDEX

Variable	Units	Description
a	m	molecular spacing along the step
a_{ij}	M	activity of solid solution end-member ij
α	J/m^2	step edge free energy per unit step height
b	m	kink depth
d	mol/m^3	solid density
ϵ	J	kink site formation energy
γ_i		activity coefficient of i
h	m	step height
I	s^{-1}	stable 1D nucleation rate
K_p		partition coefficient
K_{ij}		solubility of ij
K_{sp}		equilibrium solubility product
k_b	J/K	Boltzmann constant
k_j	$s^{-1}M^{-1}$	rate coefficient of j attachment to a kink site
ν_j	s^{-1}	rate coefficient of j detachment from a kink site
P_j		probability that a given kink site is a j site
r_x		ratio impurity and calcium carbonate in the crystal
ρ		kink density
Ω		oversaturation (IAP/K_{sp})
σ		supersaturation ($ln(IAP/K_{sp})$)
$\Sigma\Pi$	M^2	total solubility
T	K	temperature
u_j	s^{-1}	propagation rate of kink type j
v_{st}	m/s	lateral step velocity
x		mole fraction of impurity carbonate in solid solution
y		mole fraction of impurity carbonate in aqueous solution
y_0	m	step spacing or terrace width
$[j]$	M	activity of j in solution

APPENDIX B. CALCULATION OF GROWTH RATE INHIBITION BY NON-INCORPORATING IMPURITIES

The following procedure may be used to calculate precipitation rate as a function of calcium [A], carbonate [B] and impurity [M] ion concentration in solution using fitted attachment and detachment rate coefficients (k_A, k_B, k_M, ν_A, ν_B and ν_M).

- Solve for kink probabilities, P_A, P_B and P_M using Eqs. 2.14-2.16
- Calculate the net kink propagation rate by substituting kink probabilities into Eq. 2.1 for each ion. The kink propagation rate of M is 0 by definition, so

$$u_{net} = u_A + u_B = k_A[A]P_B + \nu_A P_A + k_B[B]P_A + \nu_B P_B.$$

- Calculate resistance to nucleation for A and B (Ω_A and Ω_B; Eq. 2.10).
- Determine kink density (ρ) by substituting u_{net}, Ω_A and Ω_B into Eq. 2.12 to calculate C. Substitute C into Eq. 2.11, which may be solved using the quadratic equation.
- Finally, surface normal growth rate and step velocity may be determined by inserting u_{net} and ρ into Eq. 2.6.

APPENDIX C. NUMERICAL SOLUTION OF STEADY STATE GROWTH RATE AND COMPOSITION

Both growth rate and steady state crystal composition depend on A-, B- and M-type kink propagation rates. In the case of impurity incorporation, kink probabilities cannot be calculated analytically. Instead, the constraint equations (2.3-2.5) may be solved numerically as a function of solution composition (ion activities [A], [B] and [M]) and attachment and detachment rate coefficients (k_A, k_{B-A}, k_{B-M}, k_M, ν_A, ν_{B-A}, ν_{B-M} and ν_M). We use

pseudocode to demonstrate a method for solving the system of equations using the Newton-Raphson method, but the equations may also be solved using a built-in solver such as fsolve in Matlab.

- Define inputs: ion activities, attachment rate coefficients, initial detachment rate coefficients, end-member carbonate solubilities, and thermodynamic constants (i.e. a_0).
- Initialize activity coefficients and kink probabilities: $\gamma_{AB} = 1$, $\gamma_{MB} = 0$, P_A = 0.50, P_M = 0.01 (P_B = 1 - P_A - P_M).
- For 20 iterations
  - (Re)calculate ν for A, B-A, M and B-M using Eqs. 2.31 and 2.32.
  - Pass rate coefficients and kink probabilities as values to the solver function.
    - Define step size for varying P_A and P_M (dP $\sim$ 1e-8) and step length ($\alpha \sim$ 0.2).
    - For 50 iterations
      - (Re)calculate u_M and u_A using (1) P_A and P_M, (2) P_A + dP and P_M, and (3) P_A and P_M + dP.
      - Calculate the M/A ratio of the solid for (1) - (3), where $r_x = u_M/u_A$ for each set of kink propagation rates (Eq. 2.23).
      - Calculate u_{B-A} and u_{B-M} for (1) - (3) using Eqs. 2.21 and 2.22.
      - Define errors based on Eqs. 2.3 and 2.4 for (1) - (3). For case (1),

$$E_{A1} = u_{A,1} - u_{B-A,1}$$

$$E_{M1} = u_{M,1} - u_{B-M,1},$$

        where $u_{i,1}$ is the kink propagation rate for kink type i calculated using case (1) kink probabilities.

· Calculate error sensitivity relative to changes in P_A and P_P. For example, sensitivity to changes in P_A may be expressed,

$$dE_A/dP_A = (E_{A2} - E_{A1})/dP$$

$$dE_M/dP_A = (E_{M2} - E_{M1})/dP.$$

· Define the Jacobian,

$$\mathbf{J} = \begin{pmatrix} dE_M/dP_A & dE_M/dP_M \\ dE_A/dP_A & dE_A/dP_M \end{pmatrix}.$$

· Calculate the change in kink probabilities, d**P** = $\begin{pmatrix} dP_A \\ dP_M \end{pmatrix}$, where

$$d\mathbf{P} = \mathbf{J}^{-1} \begin{pmatrix} E_{M1} \\ E_{A1} \end{pmatrix}.$$

· Update A and M kink probabilities, $P_A = P_A + \alpha\, dP_A$ and $P_M = P_M + \alpha\, dP_M$.

∗ Calculate $P_B = 1 - P_A - P_M$ using final P_A and P_M.

– Calculate kink propagation rates for A and M from Eq. 2.1 using numerically determined kink probabilities.

– Calculate the steady state M/A ratio (r_x; Eq. 2.23).

– Solve for the partition coefficient (K_p; Eq. 2.33).

– Substitute r_x into Eqs. 2.21 and 2.22 for u_{B-A} and u_{B-M}, and finally calculate u_{net}.

– Follow Appendix B directions to determine ρ, v_{st} and R.

- After 20 iterations, the calculated precipitation rate (R) and partition coefficient (K_p)

should reach steady state values.

LIST OF TABLES

Table 1: Optimized fit parameters to obtuse step velocities from Elhadj et al. (2006) experimental data, assuming $k_{Ca^{2+}} = k_{CO_3^{2-}} = k$ and $\nu_{Ca^{2+}} = \nu_{CO_3^{2-}} = \sqrt{K_{CaCO_3} k^2}$.

Asp	k $(s^{-1}M^{-1})$	k_{Asp}/ν_{Asp} (M^{-1})
1, 2	1.8e7	6.0e2

Table 2: Optimized fit parameters to obtuse step velocities from Wasylenki et al. (2005b) experimental data.

a_0	$k_{Ca^{2+}} = k_{CO_3^{2-}}$ $s^{-1}M^{-1}$	$k_{Sr^{2+}}$ $s^{-1}M^{-1}$	$k_{CO_3^{2-}-Sr^{2+}}$ $s^{-1}M^{-1}$	$\nu_{CO_3^{2-}-Sr^{2+}}/\nu_{Sr^{2+}}$	R^2
2.37	1.22e7	3.7e6	1.65e8	0.621	0.78

Table 3: Mg thermodynamic solid solution parameters. End-member solubilities and ϵ' were taken from Königsberger and Gamsjäger (1992), while γ_∞ was fitted to observed solution compositions (black $\circ$ symbols in Fig. 5).

K_{CaCO_3}	K_{MgCO_3}	ϵ'	γ_∞
$10^{-8.48}$	$10^{-6.75}$	3.69	1.2

Table 4: Fit parameters to step velocities from Astilleros (2010) experimental data, total solubility compiled in Davis et al. (2000a,b), etc.

$k_{Ca^{2+}} = k_{CO_3^{2-}}$ $(s^{-1}M^{-1})$	$k_{Mg^{2+}}$ $(s^{-1}M^{-1})$	$k_{CO_3^{2-}-Mg^{2+}}$ $(s^{-1}M^{-1})$	$\nu_{CO_3^{2-}-Mg^{2+}}/\nu_{Mg^{2+}}$
3.0e6	5.1e4	1.53e3	1.0e3

LIST OF FIGURES

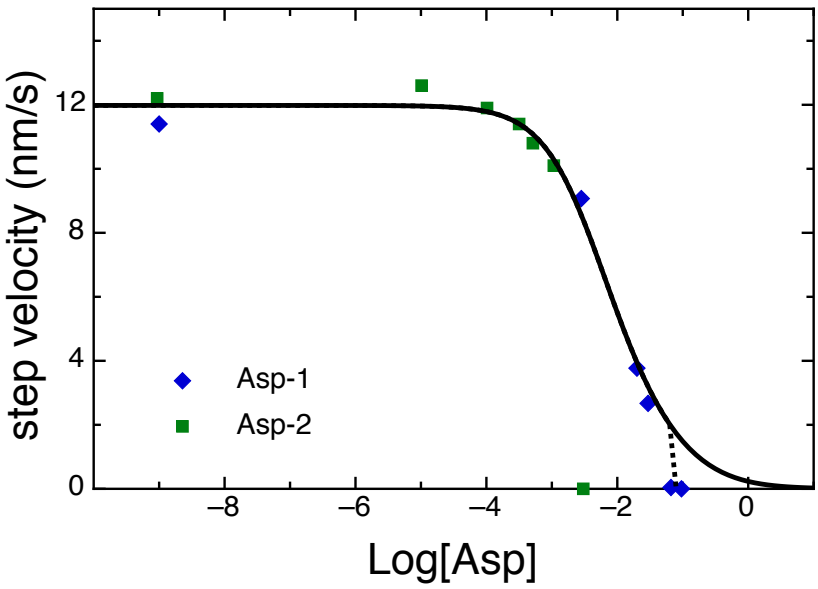

Figure 1: Calcite precipitation rate increases slightly and then decreases rapidly as a function of the concentration of polyaspartates Asp-1 and Asp-2. The solid line represents a model fit to the experimental data from Elhadj et al. (2006) using parameters listed in Table 1. Step velocity was calculated based on Eq. 2.6 using kink propagation rates determined by substituting Eqs. 2.14-2.16 into Eq. 2.1. Dashed line assumes that 1D nucleation terminates when the kink spacing is less than 2 molecular units, the approximate step width occupied by Asp-1.

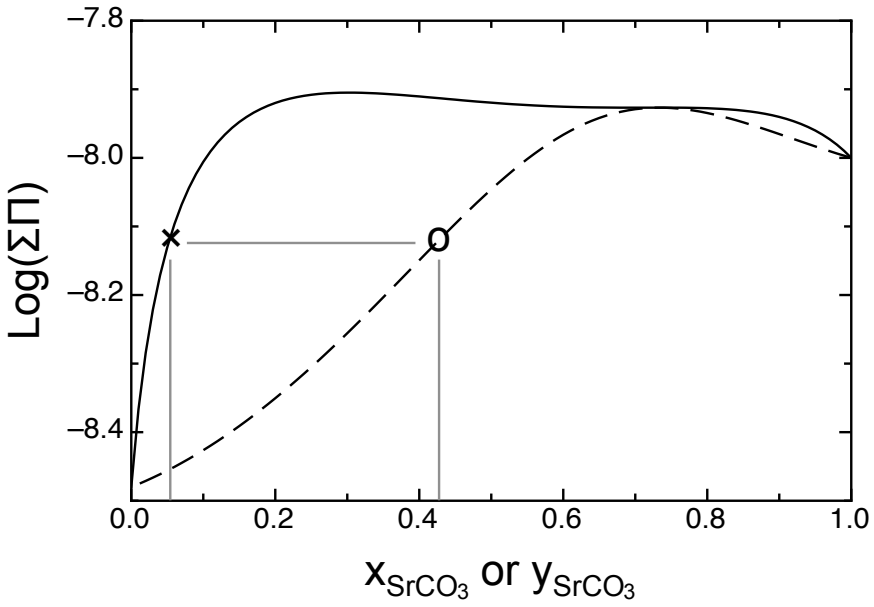

Figure 2: Lippmann diagram for the $Sr_xCa_{1-x}CO_3$ solid solution. The solid line gives the solid solution composition that would be in equilibrium with an aqueous solution (dashed line; referred to as the "solutus") for different values of total solubility. An example is shown for a solid of mole fraction $SrCO_3 = x$, which would have a total solubility log of -8.12. That solid solution composition would be in equilibrium with an aqueous solution with analogous mole fraction y shown by the small circle. Note that as y_{SrCO_3} approaches 0.8, the solid has a miscibility gap. This represents the point where Sr-bearing $CaCO_3$ ceases to grow as the Sr/Ca ratio of the solution in increased (see Fig. 3b).

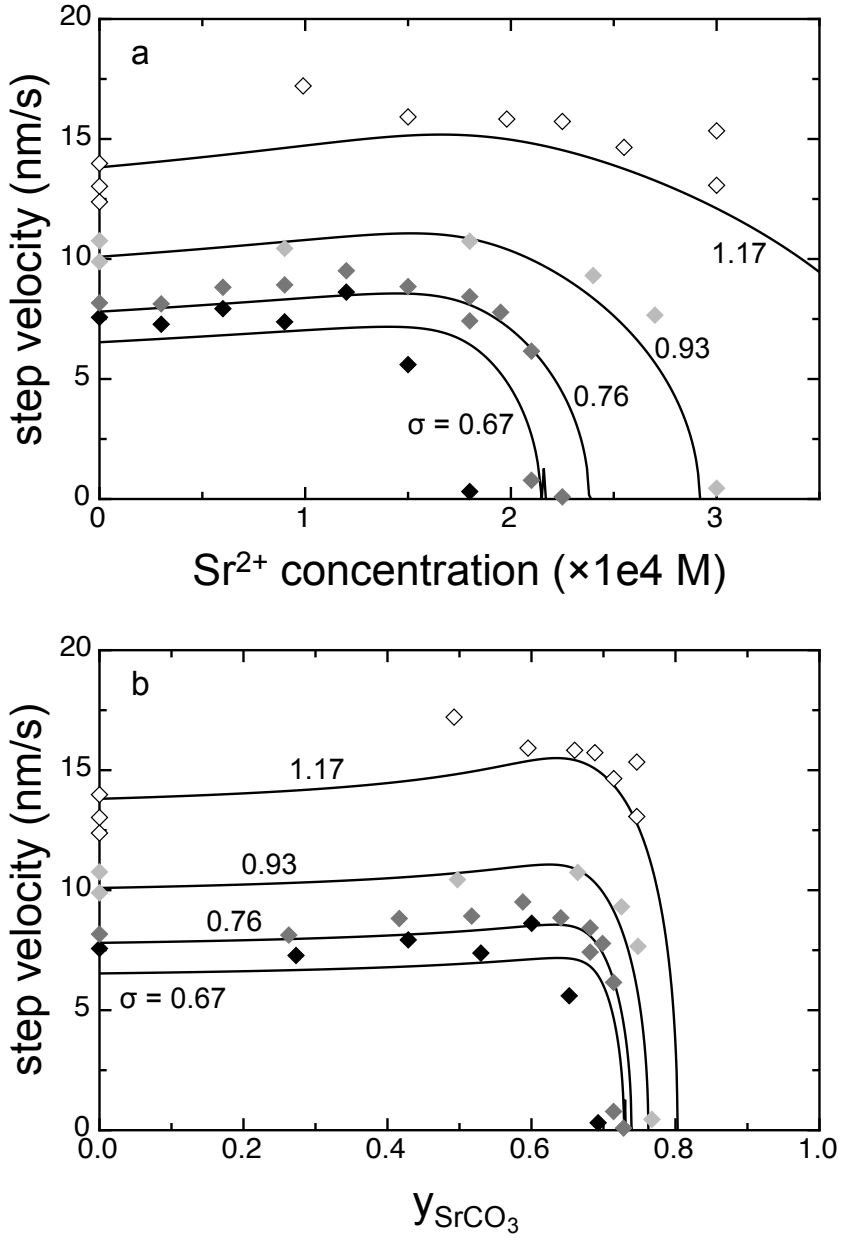

Figure 3: Obtuse step velocities optimized as a function of a) [Sr^{2+}] and b) y_{SrCO_3} for a kinetic end-member fractionation factor of 0.3. The fit was optimized using the Levanburg-Marquardt algorithm to data from Wasylenki et al. (2005b), with a final R^2 value of 0.78.

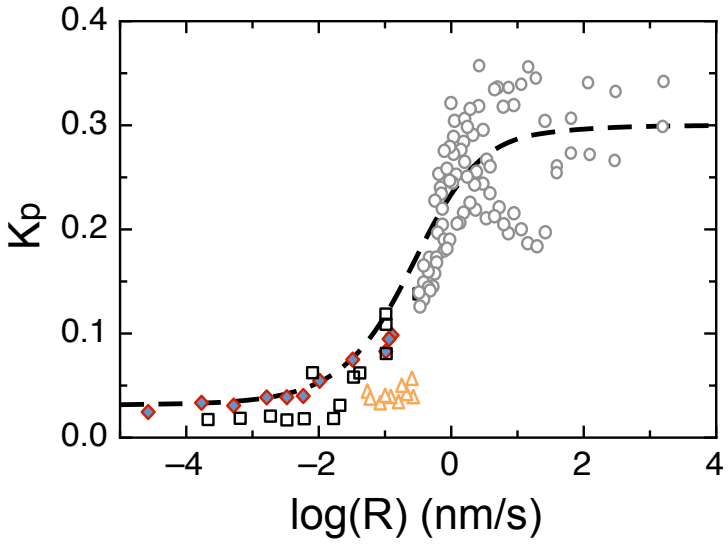

Figure 4: Partition coefficients optimized for a kinetic end-member partition coefficient of 0.3 modeled as a function of surface normal precipitation rate (nm/s). Literature data are compiled from (Gabitov and Watson, 2006, circles and triangles), (Lorens, 1981, diamonds), (Tesoriero and Pankow, 1996, squares)

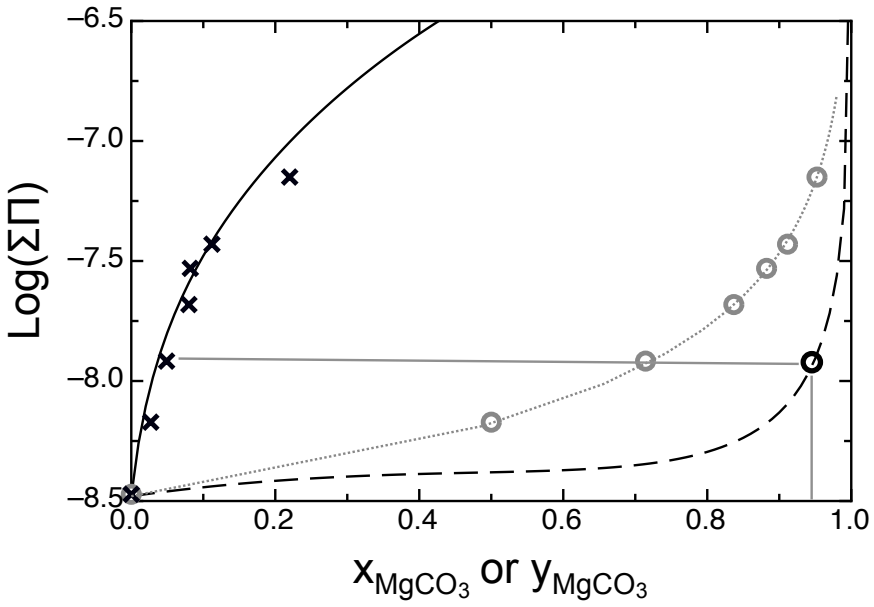

Figure 5: Lippmann diagram of magnesian calcite total solubility as a function of mole fraction of $MgCO_3$ in the solid solution (x_{MgCO_3}), which is represented by the solidus line (solid line), and mole fraction of aqueous magnesium in solution (y_{MgCO_3}), which is represented by the solutus line (dashed). The solution with the composition denoted by the black circle is tied (gray horizontal line) to the corresponding equilibrium solid x_{MgCO_3}. Experimentally precipitated solid $Mg_xCa_{1-x}CO_3$ compositions and corresponding solution compositions from Mucci and Morse (1984) are represented by black $\times$ and gray $\circ$ symbols. The modeled total solubilities of solid and aqueous solution compositions based on the Mucci and Morse (1984) results are marked as solid black and dotted gray lines respectively. The Mucci and Morse (1984) data (gray circles and grey dotted line) do not match the equilibrium solution compositions (black dashed line). This means that Mucci and Morse (1984) did not manage to precipitate calcite at equilibrium in their experiments, which is not surprising.

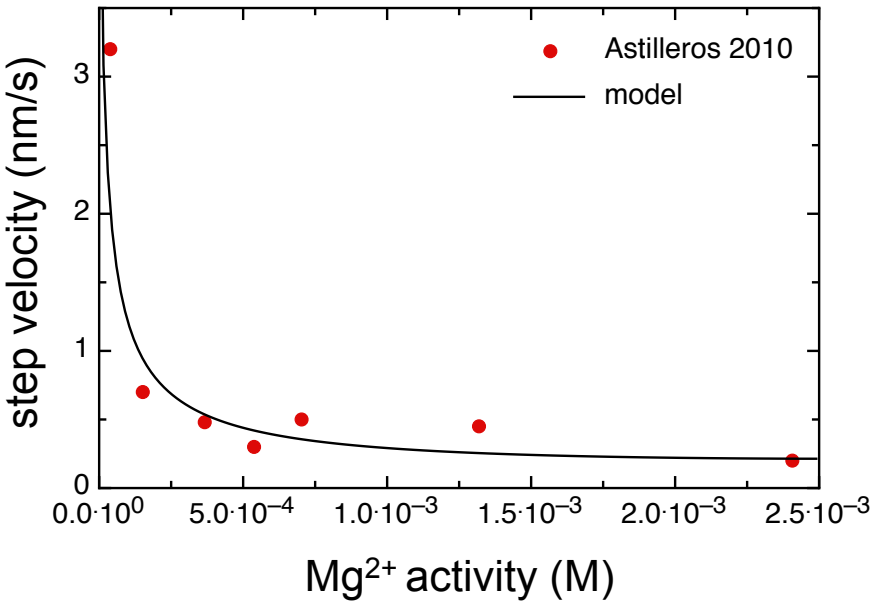

Figure 6: Modeled step velocity as a function of magnesium activity during calcite precipitation from oversaturated solution (σ = 1.6) with Ca^{2+}:CO_3^{2-} = 1 from Astilleros et al. (2010). Fitted kinetic coefficients are listed in Table 4 and thermodynamic data are listed in Table 3.

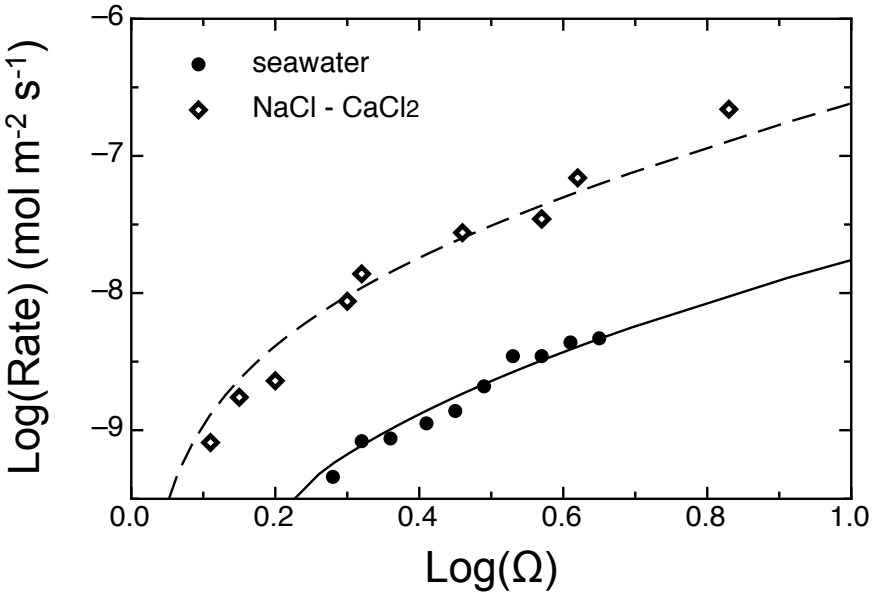

Figure 7: Calcite precipitation rates from NaCl - $CaCl_2$ solutions and seawater solutions as a function of calcite supersaturation reported by Lopez and Zuddas (2009). Rate data from NaCl - $CaCl_2$ solutions were fitted by setting $(Mg^{2+}) = 0$ (dashed line) , and data from seawater were fitted using the reported $Mg^{2+}/Ca^{2+} = 5.4$ (solid line). Both model fits use the same thermodynamic and kinetic coefficients listed in Tables 3 and 4, except the kinetic coefficients for ion attachment were all increased by a factor of 2.8 to fit the observed growth rates from seawater (solid line). Both models use a calcium activity $[Ca^{2+}] = 0.002$ equal to the approximate seawater value (Berner, 1965) with varied $[CO_3^{2-}]$. This plot shows that our model for growth inhibition of calcite by Mg is in accord with experimental data.

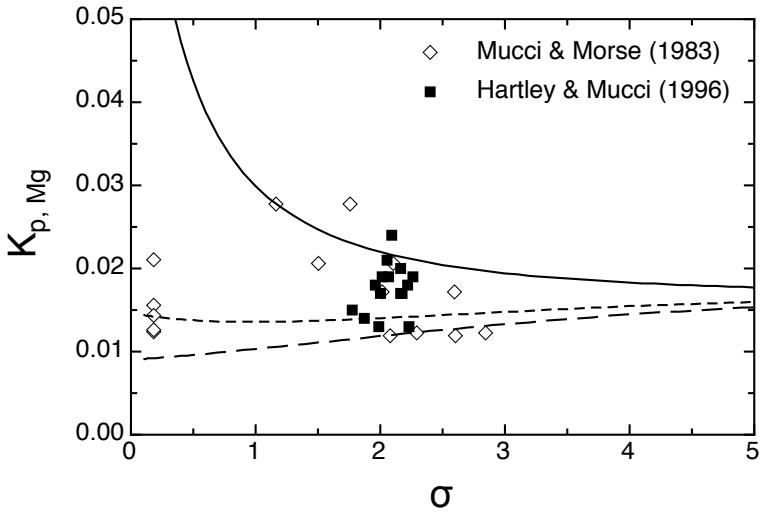

Figure 8: Modeled magnesium partition coefficient as a function of supersaturation with respect to calcite ($\sigma = \log(\mathrm{IAP}/\mathrm{K_{sp}})$). Typical measured magnesium partition coefficients during precipitation from seawater vary from 0.01 to 0.03, and estimated equilibrium partition coefficients range from $\sim$0.001 to 0.03 (Huang and Fairchild, 2001; Fantle and DePaolo, 2006). Fitted kinetic and thermodynamic parameters are the same as those listed in Tables 3 and 4, with the exception of γ_∞, which is varied from 0.1 (solid line) to 2 (lower dashed line). Magnesium partitioning modeled using parameters fitted to step velocity and total solubility data (γ_∞ = 1.2) is represented by the upper dashed line.

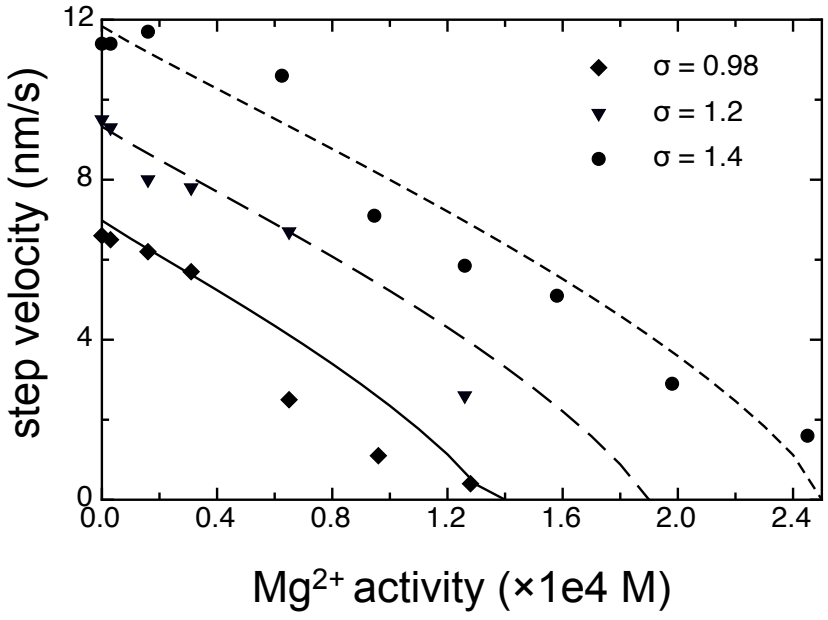

Figure 9: Fit to Davis (2000) obtuse step velocities using their reported IAP values. Detachment rate coefficients for Mg and Ca are assumed to be equal. Activities calculated from attachment and detachment rate coefficients violate the Gibbs-Duhem relation.

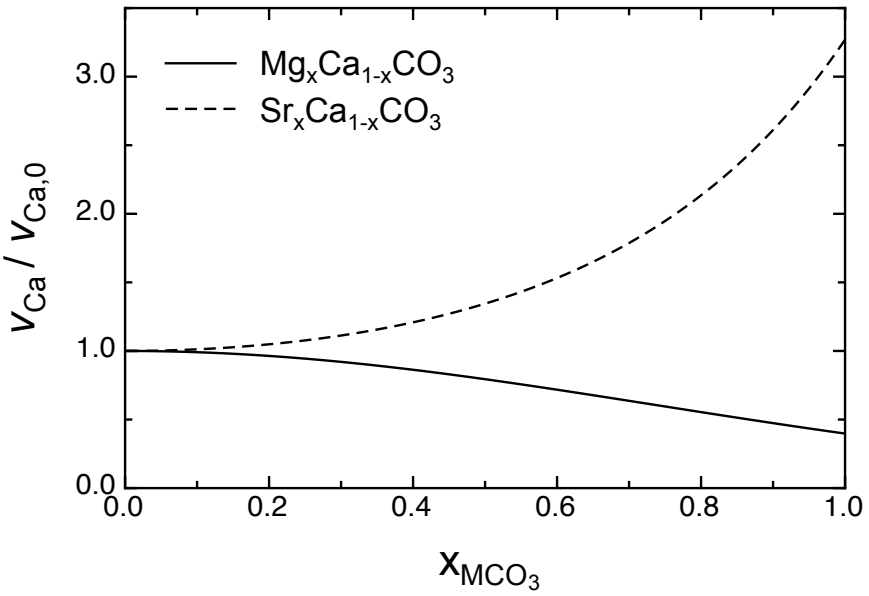

Figure 10: Detachment rate coefficients for calcium calculated as function of $SrCO_3$ and $MgCO_3$ mole fraction in the solid solution, normalized to the $\nu_{Ca^{2+}}$ of pure calcite. Adding Sr to calcite tends to increase the Ca detachment rate, eventually making calcite undersaturated and thereby stopping growth. The addition of Mg does not increase the detachment, so there is no increase in calcite solubility, and hence calcite remains stable in solution but its growth rate slows abruptly due to kink blocking.